

## Can a DNA Origami Structure Constrain the Position and Orientation of an Attached Dye Molecule?

Divita Mathur, Young C. Kim, Sebastián A. Díaz, Paul D. Cunningham, Brian S. Rolczynski, Mario G. Ancona, Igor L. Medintz, and Joseph S. Melinger\*



Cite This: *J. Phys. Chem. C* 2021, 125, 1509–1522



[Read Online](#)

## ACCESS ||



Metrics & More

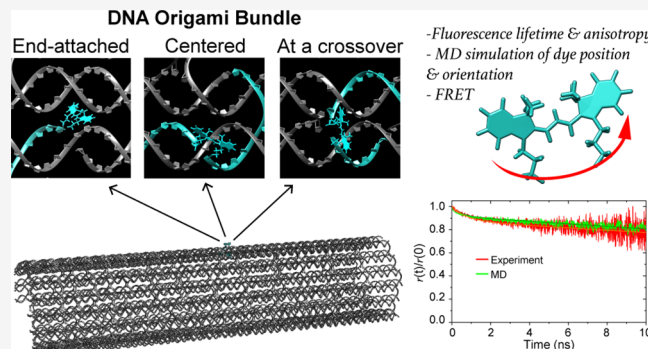


## Article Recommendations



## Supporting Information

**ABSTRACT:** There has been significant interest in using DNA origami nanostructures as scaffolds to organize dye molecules into networks for a variety of applications. Such networks rely on having efficient energy—and/or electron—transport processes, and these in turn depend sensitively on the relative distance and orientation of the dye molecules. In using DNA as a scaffold, a crucial question is to what extent can it control the dye position and orientation? The ability of DNA nanostructures to dictate the position is reasonably well addressed in the literature, but much less is known about the potential for controlling the orientation and its dependences on the local rigidity of the DNA, on the dye attachment chemistry, and on other aspects of the local microenvironments of the dye. To investigate these issues, we here employ a Cy3 probe dye and use its measured fluorescence which a DNA duplex and a 30-helix DNA origami bundle can provide the excited state lifetimes and rotational anisotropy decays are longer more constrained in the former. Atomistic molecular dynamics (MD) further provide insight into how the microenvironment of the bundle transfer simulations based on the MD data indicate that the conditions substantially raise the transfer efficiency (over the duplex) if the site of this work should be useful for improving the performance of DNA



properties and numerical simulations to compare the degree to which the desired control over the dye. Experimentally, we find that it is easier for the bundle than for the duplex indicating that the Cy3 is more constrained (MD) simulations are found to be in good agreement, and they show that it is limiting the dye motion. Moreover, Förster resonance energy transfer constraints imposed by the DNA bundle can be sufficient to ensure that the coupling of the donor and acceptor is well chosen. Overall, the results show that the use of DNA-scaffolded dye networks.

## ■ INTRODUCTION

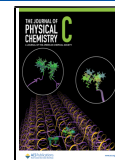
Synthetic DNA nanostructures have emerged as versatile structures for the positioning of a variety of organic and inorganic molecules such as gold nanoparticles,<sup>1–3</sup> enzymes,<sup>4</sup> and fluorescent dyes.<sup>5–8</sup> In the case of dye molecules, a variety of DNA-organized photonic wires and 3D networks have been assembled to gather and transmit photonic energy in a biomimetic fashion motivated by highly efficient biological light harvesting (LH) antennas.<sup>7–18</sup> In this application, the chemical addressability of DNA is exploited to attach the dyes to specific sites with a spatial resolution approaching 1 nm.<sup>19</sup> In some cases, this has led to efficient energy transfers over distances as large as about 30 nm.<sup>12,17,20,21</sup> However, it is often found that the measured energy transfer efficiencies in such multidye/DNA networks are smaller than those predicted by the Förster theory.<sup>7,8,12</sup> One reason for this is the presence of nonidealities in the dye–DNA networks, due to the absence or bleaching of dyes, imperfections in the DNA assembly, etc.<sup>8</sup> A second contributor is inadequacy in the DNA's control of the dye positions<sup>8,12,22</sup> and/or orientations, and this is the focus of the present investigation.

Understanding whether and how a DNA nanostructure might control dye positioning and orientation is critical if a DNA-scaffolding approach is to be successful in creating highly efficient synthetic organic materials for photonic applications. The challenge is best appreciated by comparing with biological LH systems in which networks of chlorophylls, carotenoids, or other pigments transfer energy to a reaction center with near 100% efficiency.<sup>23</sup> The key to achieving this performance is the protein scaffolds that control the positions and orientations of the chromophores, yet, to date, the *de novo* design of peptide/protein structures is very limited. Can structural DNA methods provide an analogous functionality for a synthetic LH technology? In particular, is a DNA origami nanostructure stiff enough to be a good photonic scaffold and can it

**Received:** October 12, 2020

**Revised:** December 2, 2020

**Published:** December 23, 2020



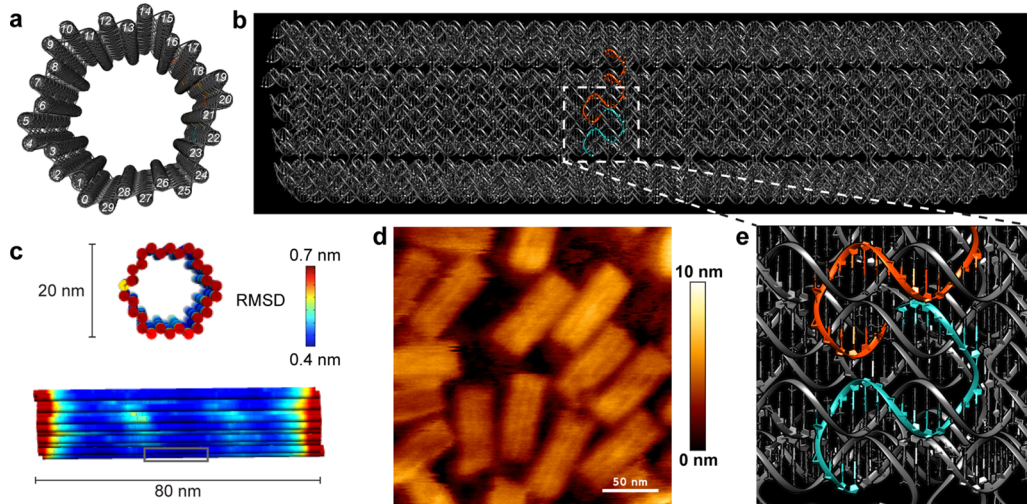


**Figure 1.** Schematic of the DNA bundle. Ribbon rendering of the DNA bundle in (a) front view and (b) side view. The white dashed box in the side view highlights the staple sites to which Cy3 was coupled. (c) CanDo analysis of the DNA bundle wherein the heat map shows the root mean square deviation (RMSD) fluctuations within the structure. The gray box indicates the region where Cy3 was placed. (d) Representative AFM image of the DNA bundles. (e) Higher resolution representation of the staple strands (orange and blue) within the DNA bundles that were modified to contain Cy3. The blue staple (25 bp) was modified in structures A, C, and E whereas the orange staple (45 bp) was modified in structures B, D, and F.

sufficiently restrict the relative motion of a dye both translationally and rotationally using the covalent attachment schemes in current use? While this paper cannot provide complete answers to these questions, our purpose is to work toward this goal.

To address the foregoing questions experimentally, one would need to assemble a variety of dye-labeled DNA origami structures and then characterize them in detail at a molecular scale. Unfortunately, at present, the techniques available for physically characterizing the DNA structures are inadequate for this purpose, especially when our interest is in the behavior at room temperature in aqueous media for which cryo-transmission electron microscopy (TEM) methods are not relevant. Ordinary TEM and atomic force microscopy (AFM) methods are of course available, but the former works with dry samples<sup>24</sup> and the latter is sample-invasive and lacks resolution. We are therefore left with indirect spectroscopic methods such as fluorescence lifetime and anisotropy measurements, and these are central to the investigation presented here. We complement these with extensive atomistic molecular dynamics (MD) simulations that, when based on well-calibrated models, provide direct estimates of the range of positions and orientations of a dye within a DNA nanostructure as well as information about the localized dye microenvironment.<sup>25–31</sup> An example of the importance of such modeling can be found in a recent report that observed that cyanine (Cy5) dyes conjugated to end nucleotides surprisingly outperformed dyes doubly attached to internal nucleotides in Förster resonance energy transfer (FRET) efficiency.<sup>32</sup>

As our testbed for probing the ability of a DNA nanostructure to control the position and orientation of a covalently linked dye, we use a 30-helix DNA origami bundle (see Figure 1). Convenient sites for inserting dyes are the 3' and 5' ends of staple strands, by either replacing the end base (i.e., with attachment to the second-to-end base) or coupling to the terminal base directly. We also considered internal dye attachments at crossover sites and at locations farthest from crossovers in order to compare local structural rigidity as a

factor in dye localization. To keep the study manageable, we focus on Cy3 as our prototypical dye because it is one of the most commonly used dyes in DNA photonics, exhibits fluorescence lifetimes that depend on the surrounding environment, and is amenable to many DNA conjugation linkages.<sup>33,34</sup> However, it should be recognized that this limits the generality of our results, especially for dyes outside the cyanine family. In any event, to explore the possibilities, we assembled six distinct Cy3-labeled DNA bundles with varying dye attachment locations and chemistries. In addition, as controls, we created analogues to each bundle in the form of DNA duplexes (dsDNA) in which the dye-conjugated strands were hybridized with their complements. In each sample, the Cy3 confinement was characterized by measuring its fluorescence lifetime and time-resolved fluorescence anisotropy. The Cy3 fluorescence lifetime depends on the dye's propensity to undergo photoisomerization,<sup>34</sup> and therefore, provides a sensitive probe of local constraints.<sup>35,36</sup> As already noted, we parallel the experiments with atomistic MD simulations and use these to help interpret the data as well as estimate the FRET efficiency in a modeled Cy3–Cy5 dye pair in different configurations.

Our experimental results show clear differences in the Cy3 fluorescence dynamics when the dye is attached to the six different DNA bundles and to their corresponding dsDNA analogues. The bundles displayed up to 2.3-fold longer fluorescence lifetimes as well as generally a slower decay in the time-resolved fluorescence anisotropy when compared to the dsDNA controls. Atomistic MD simulations of selected bundles and dsDNA analogues were found to be in excellent agreement with these experimental measurements, and on this basis, were used to provide physical understandings for the reduced dye motions that were observed. Among other things, we could distinguish the contributions to the relaxation of the overall tumbling of the DNA nanostructure as a whole, the internal motions of the DNA, and the particular dye motions allowed by their flexible linkers. It was found that positioning of the Cy3 at a crossover site within the bundle provided the

greatest restriction on the dye motion, whereas end attachments gave the narrowest distributions of dye orientations. Finally, the dye motion obtained from the MD simulations was used to simulate FRET in a model system, and we found that the enhanced control provided by the DNA bundle over the dye position and orientation was indeed sufficient to provide significant boosts in FRET efficiency in certain optimal cases.

## MATERIALS AND METHODS

**DNA Bundle and dsDNA Sample Preparation.** All unlabeled staple strands were purchased from Integrated DNA Technologies (IDT, Coralville, IA), each at 100  $\mu\text{M}$  in RNase-free water (Table S8). Cy3-conjugated A–F strands were purchased from IDT in a lyophilized state and were reconstituted to 100  $\mu\text{M}$  in molecular biology grade water before use. The scaffold strand (m13mp18 single-stranded DNA) used for the DNA bundle assembly was purchased from Bayou Biolabs (Harahan, LA) at 500  $\mu\text{g}/\mu\text{L}$  and used without further processing.

DNA bundles were assembled by combining a 20 nM scaffold strand with 100 nM of each staple strand in 50 mM HEPES pH 7.5 + 9 mM MgCl<sub>2</sub> and subjected to the following thermal anneal process: 85 °C for 5 min, 85 to 60 °C at 5 min/°C, 60 to 25 °C at 15 min/°C, 25 to 4 °C at 5 min/°C, and 4 °C until further use. dsDNA analogues were prepared by mixing equimolar amounts of the Cy3 strand (A–F) and the corresponding complementary strand (25 or 45 bp) at a final concentration of 200 nM and using the same thermal anneal program.

The purification of DNA bundles was performed using Amicon ultracentrifugation size-exclusion columns (100 kDa molecular weight cutoff). A volume of 5000  $\mu\text{L}$  at 20 nM of each sample was loaded into a 15 mL filter column (column loading capacity 4 mL) and subjected to centrifugation at the maximum speed for 10 min. After discarding the elute, more sample was added to the same column until the entire sample was spun down. The retained sample postcentrifugation was recovered and further purified using 2 mL ultracentrifugation columns with 6–7 buffer rinses and subjected to centrifugation at 9000g each time for 4 min. Finally, the column was inverted into a clean 2 mL vial and the purified sample was recovered by spinning at 3000g for 3 min. The DNA bundle concentration after purification was calculated using absorption at 260 nm with an assumed extinction coefficient of  $1 \times 10^8 \text{ M}^{-1} \text{ cm}^{-1}$ .<sup>37</sup>

**Steady-State Measurements.** Steady-state absorption spectra were measured using 120  $\mu\text{L}$  of each sample in a 10 mm path length cuvette with an Agilent 8453 diode array UV-vis spectrophotometer. Excitation and emission spectra were measured using 60  $\mu\text{L}$  of each sample loaded into a Corning black flat-bottom 96-well plate in a multifunction microtiter plate reader (Tecan Infinite M1000 Pro) with excitation at 520 nm. The excitation and emission spectra were corrected for wavelength dependent instrumental effects.

**Fluorescence Anisotropy and Lifetime Measurements.** Fluorescence lifetimes ( $\tau$ ) and lifetime anisotropies were measured using the time-correlated single photon counting (TCSPC) technique using a Becker–Hickl SPC-630 board.<sup>17,18</sup> The excitation laser was a 515 nm diode laser (Becker–Hickl) operating at 50 MHz and with a FWHM pulse width of approximately 80 ps. Sample fluorescence was sent through a polarizer set to the magic angle for lifetime determination and then filtered using a monochromator and detected using a microchannel plate photomultiplier. The

polarizers were adjusted to the pertinent parallel and perpendicular settings to obtain the fluorescence anisotropy using

$$r(t) = \frac{I_{\parallel} - G \times I_{\perp}}{I_{\parallel} + 2G \times I_{\perp}}, \quad (1)$$

where  $I_{\parallel}$  and  $I_{\perp}$  are the parallel and perpendicular components of the fluorescence as measured with respect to the laser polarization and  $G$  is the correction factor to account for the polarization dependence of the detection system.

**Molecular Dynamics Simulation.** The molecular model for the DNA bundle was generated using CanDo (MIT, MA) to which was then added the Cy3 dye at the A, E, or F sites using Chimera (UCSF, CA).<sup>38</sup> For the purpose of computational efficiency in the MD simulations, the full DNA bundles were truncated to include only a region spanning ~40 Å around the Cy3 in the A<sub>bundle</sub>, E<sub>bundle</sub>, and F<sub>bundle</sub> structures. Molecular models for A<sub>dsDNA</sub>–Cy3 and E<sub>dsDNA</sub>–Cy3 were built entirely in Chimera. The atomistic MD simulations were performed using the Gromacs 5.1.5 package<sup>39</sup> on DNA–Cy3 structures using Amber99sb force field parameters<sup>40</sup> for DNA and “GAFF”<sup>41</sup> for Cy3. Atomic net charges for Cy3 were calculated so as to reproduce the electrostatic potential with the HF/6-31G\* level. The starting structures were then solvated using the TIP4P-Ew water model<sup>42</sup> in a truncated octahedral box for dsDNA–Cy3 and in a triclinic box for bundle–Cy3 structures using a 15 Å buffer distance between the solute and the edge of the box. Periodic boundary conditions were employed for all simulations. Then, 9 mM MgCl<sub>2</sub> was introduced to neutralize the system and match the experimental conditions. The long-range electrostatics was computed using the particle-mesh Ewald method with a real-space Coulomb cutoff of 1.2 nm. The van der Waals interactions were cut off at 1.2 nm. All bonds were constrained using the LINCS algorithm.<sup>43</sup> The neighbor-searching algorithm was used with a cutoff of 1.2 nm, and the neighbor list was updated every tenth step. A timestep of 2 fs was used for all simulations.

The systems were energy-minimized using the steepest descent method for 10,000 steps. For the bundle–Cy3 constructs, the systems were first equilibrated for 100 ps without any constraints at 300 K and a pressure of 1 atm. After initial relaxation, harmonic constraints with a spring constant of 100 kJ/mol/nm<sup>2</sup> were applied to some of the P atoms at the edge of the bundle to prevent the system from tumbling. The systems for both bundle–Cy3 and dsDNA–Cy3 were then equilibrated for 1 ns at a constant temperature of 300 K and a pressure of 1 atm. The velocity rescale thermostat<sup>44</sup> was used at 300 K with a coupling constant of 0.1 ps applied to Cy3–DNA and water separately. The pressure was maintained at 1 atm isotropically using the Parinello–Rahman barostat<sup>45</sup> with a coupling constant of 1.0 ps. The production trajectories of the Cy3–DNA complexes were calculated for 500 ns, keeping the number of particles, temperature, and pressure constant. The coordinates were written every 10 ps. The last 400 ns of the trajectories were then selected for further analysis.

For a discrete time trajectory of the normalized transition dipole vector,  $\hat{\mu}(i\delta t)$ ,  $i = 0, 1, \dots, N_{\max}$  with  $\delta t$  being the time between two neighboring configurations, the normalized anisotropy was calculated as

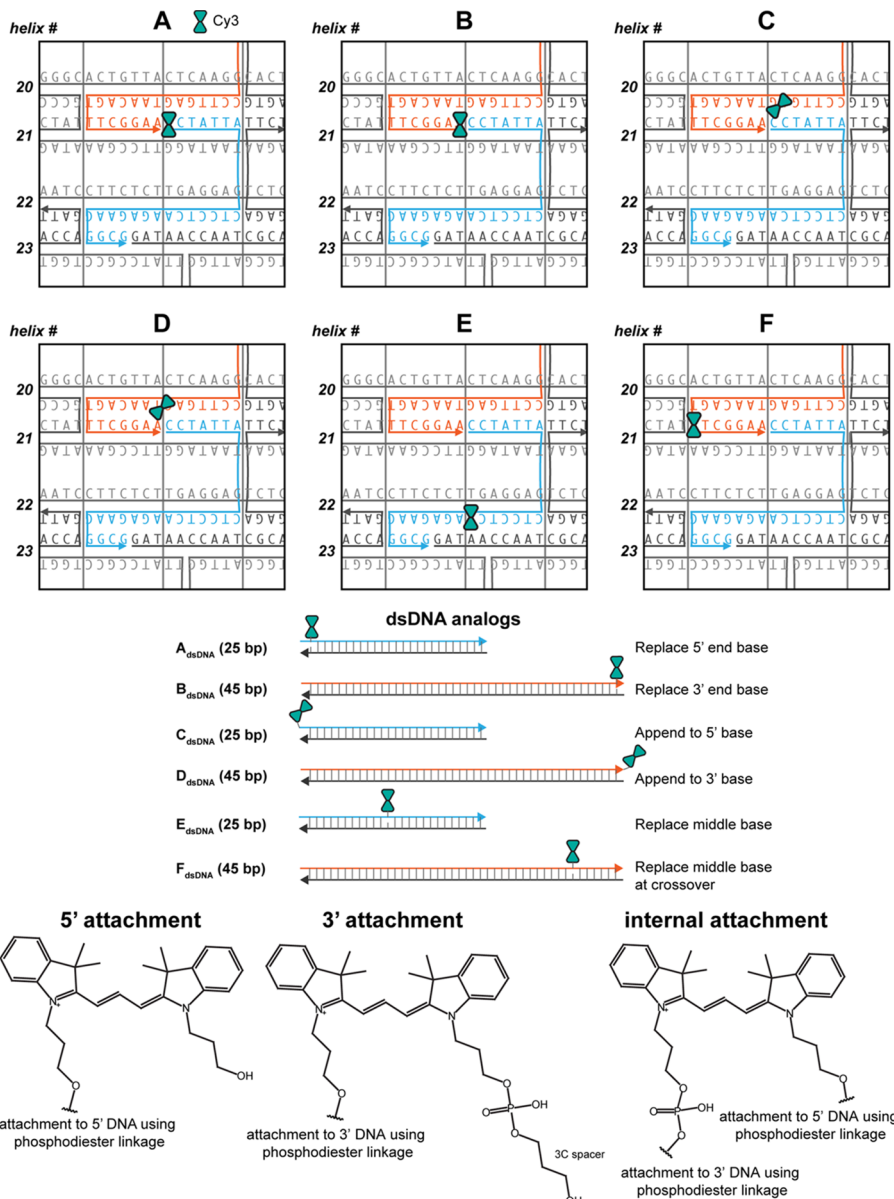


**Figure 2.** Schematic describing the Cy3 structures tested on the DNA bundle and the corresponding dsDNA analogues. For each structure, a close-up caDNAno snapshot of the DNA bundle (based on Figure 1e) is shown to highlight the Cy3 (blue bow) conjugation site. Arrow heads represent 3' DNA ends. (A) 5' attachment replacing the end base, (B) 3' attachment replacing the end base, (C) 5' attachment coupled to the end base, (D) 3' attachment coupled to the end base, (E) internal attachment replacing a base away from crossovers, and (F) internal attachment replacing a crossover base. 2D representation of Cy3–DNA attachment chemistries. Left: 5' end attachment, middle: 3' end attachment, and right: internal double phosphodiester attachment.

$$\frac{r(i\delta t)}{r(0)} = \frac{1}{N} \sum_{n=0,j}^{N_{\max}} P_2[\hat{\mu}(n\delta t + i\delta t) \cdot \hat{\mu}(n\delta t)] \quad (2)$$

where the summation was performed at every  $j$ th step, that is,  $n = 0, j, 2j, \dots$  and  $N$  is the normalization factor. Here, we set  $j = \min(i, M)$ , with  $M\delta t = 10 \text{ ns}$ . This procedure reduces the systematic error from highly correlated data points at short times as well as statistical error from the scarcity of data points at long times.

## RESULTS AND DISCUSSION

**Design and Assembly of the DNA Bundle.** The DNA bundle was chosen as a scaffold for this work because of its high structural stability and its relative rigidity. Its basic

structure is that of a DNA origami in which a long single-stranded template DNA, referred to as the scaffold strand, is folded into a predetermined shape using a pool of complementary short synthetic oligonucleotides called staple strands.<sup>46</sup> The folding process occurs via a series of Holliday junction isomers called crossovers that link the constituent strands and that guide the formation of the desired DNA origami structure. Our particular bundle design consisted of a 30-helix hollow cylinder that was laid out using the honeycomb lattice format in the design software caDNAno<sup>47</sup> (Figure 1a,b). The DNA bundle was composed of 225 staple strands (Figure S1), of which two adjacent staples were singled out for the dye attachments in the six implemented design configurations (Figure 1e). As a first assessment of the DNA bundle structure (without dyes), we used the finite element code in CanDo

(<https://cando-dna-origami.org/>) to generate a map of the root mean square fluctuations (RMSF) in the structure in its initial unrelaxed state (Figure 1c). From this map, we identified a promising segment (marked with a gray box in Figure 1c) of the bundle where the fluctuations were relatively minimal.

For generating the six bundles with different dye configurations, the labeled staple strands had the Cy3 attached as follows: (A) at the 5' end replacing the end base, (B) at the 3' end replacing the end base, (C) at the 5' end coupled to the end base, (D) at the 3' end coupled to the end base, (E) internally replacing a base away from the crossovers, and (F) internally replacing a base at a crossover. Figure 2 shows the schematics of the six bundles, their dsDNA counterparts, and the attachment chemistries used for 5', 3', and internal dye-DNA conjugation (see the Supporting Information for the base sequences). The three linker chemistries vary slightly according to what is available commercially with the 5' end attachment requiring a single phosphodiester linkage, the 3' end attachment requiring a single phosphodiester linkage but including an additional propyl group on the distal side of the dye, and the internal attachment using a double phosphodiester linkage of the dye to the backbone of the oligonucleotide. The microenvironment around the dye is determined by both the sequence in the vicinity of the dye and the local layout of crossovers and strand ends. The microenvironment is best preserved in structures A–D where the 5' and 3' attachment points were chosen to be next to each other. In contrast, structures E and F compared the internal dye attachment when the dye was located either (E) far from or (F) near the Holliday junction. It should be noted that these locations differed not only in their distance from the junction but also in their local base sequences. Linear strands complementary to the dye-labeled staples were also generated (Table S1), and the DNA duplexes so generated (Figure 2) represent the control structures ( $A_{\text{dsDNA}}-F_{\text{dsDNA}}$ ) with the same sequences and dye attachments as in the corresponding bundles ( $A_{\text{bundle}}-F_{\text{bundle}}$ ).

Bundle samples were assembled and purified as described in the Materials and Methods section. Initial characterization was performed by AFM and this demonstrated that the bundles assembled as desired and efficiently (Figure 1d). The dsDNA controls were assembled and utilized without further purification as the duplex assembly was assumed to occur with nearly 100% efficiency.

**Steady-State Spectroscopy.** Steady-state absorption, excitation, and emission spectra were measured at room temperature for the purified Cy3-labeled bundles ( $A_{\text{bundle}}-F_{\text{bundle}}$ ) and their corresponding dsDNA ( $A_{\text{dsDNA}}-F_{\text{dsDNA}}$ ) structures. Figure S2 shows the normalized absorption and fluorescence spectra, and Figure S3 shows the normalized fluorescence excitation spectra. Figure 3 and Table S2 compare the peak absorption ( $\lambda_{\text{abs}}^{\text{peak}}$ ) for each structure. The Cy3 absorption lineshape is similar for all, though there are variations in  $\lambda_{\text{abs}}^{\text{peak}}$  that are likely related to differences in the Cy3 microenvironments and/or methods of attachment. The bundle structures generally show  $\lambda_{\text{abs}}^{\text{peak}}$  that is red-shifted relative to that of the corresponding dsDNA analogues with  $F_{\text{bundle}}$  having the reddest (longest wavelength)  $\lambda_{\text{abs}}^{\text{peak}}$  at 553 nm. Interestingly, the main absorption band (centered near 550 nm) of  $F_{\text{bundle}}$  is slightly narrower than the corresponding main bands of the other bundle structures (e.g., the half width at half maximum for  $F_{\text{bundle}}$  is  $\sim 10.7$  nm, compared to  $\sim 12.0$  nm for the  $A_{\text{bundle}}$ ). The band shapes of the Cy3–bundle excitation

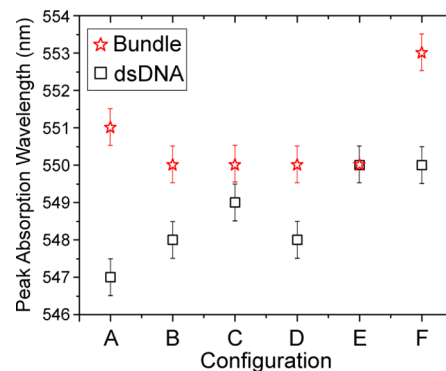


**Figure 3.** Comparison of peak absorption wavelength for each dsDNA and bundle configuration.

spectra (Figure S3) agree well with the absorption spectra (Figure S2), which indicates that the ensemble of bundles in solution is homogeneous. The fluorescence spectra (Figure S2) of  $A_{\text{dsDNA}}-F_{\text{dsDNA}}$  and  $A_{\text{bundle}}-F_{\text{bundle}}$  show somewhat less variation in the peak wavelength ( $\lambda_{\text{em}}^{\text{peak}}$ ) than the absorption spectra, with the reddest  $\lambda_{\text{em}}^{\text{peak}}$  occurring for  $F_{\text{bundle}}$  (Table S2).

**Time-Resolved Fluorescence Lifetimes and Anisotropy.** Figure 4a–c shows the time-resolved fluorescence for all the structures. The average fluorescence lifetimes ( $\langle \tau_f \rangle$ ) (weighted amplitude average) are determined by fitting the experimental curves to a decay function that is the sum of two or three exponentials, as shown in Figure 4c. The amplitudes and time constants from the curve fitting are listed in Table S3. Overall, the  $\langle \tau_f \rangle$  values for the bundles were longer by up to a factor of 2.3 when compared to the corresponding dsDNA analogues. The relative increase in  $\langle \tau_f \rangle$  was largest for case A (2.3-fold) and nearly equivalent between bundle and dsDNA for type E, while the  $F_{\text{bundle}}$  had the longest  $\langle \tau_f \rangle$  of  $2.25 \pm 0.10$  ns. Time-resolved fluorescence anisotropy for the dsDNA and bundle structures is shown in Figure 4d,e, and again, we see much slower decays in the bundles. To aid in interpreting these dynamics, we analyzed the decay curves with an expression for the normalized anisotropy that has been used previously to describe the librational motion in macromolecules.<sup>48,49</sup>

$$\frac{r(t)}{r(0)} = S^2 \exp\left(-\frac{t}{\tau_M}\right) + (1 - S^2) \exp(-t(\tau_e^{-1} + \tau_M^{-1})) \quad (3)$$

where  $\tau_M$  describes the slow anisotropy decay associated with the Cy3 motion that accompanies the DNA motion, while  $\tau_e$  is the faster relative motion of the Cy3 dye within the macromolecule. The quantity  $S^2$  is thus a measure of the extent to which the DNA motion determines the anisotropy decay with  $S^2 = 1$  corresponding to the case where the relative motion of the Cy3 plays no role and  $S^2 = 0$  being the case when the relative motion dominates. Figure 4f shows an example of using eq 3 to fit the anisotropy decay of  $F_{\text{bundle}}$ . Figure 4g–i displays the values of  $S^2$ ,  $\tau_e$ , and  $\tau_M$  obtained from similar fittings of all the experimental data, and Table S4 gives a summary. The most significant difference seen in the anisotropy dynamics was in  $\tau_M$  with the bundle values being several times larger than those for dsDNA. The values of  $\tau_e$  also tended to be longer for the bundle, with the only exception being case E. For each of the cases (A–F), the  $S^2$  restriction parameter was always larger for the bundle than for the

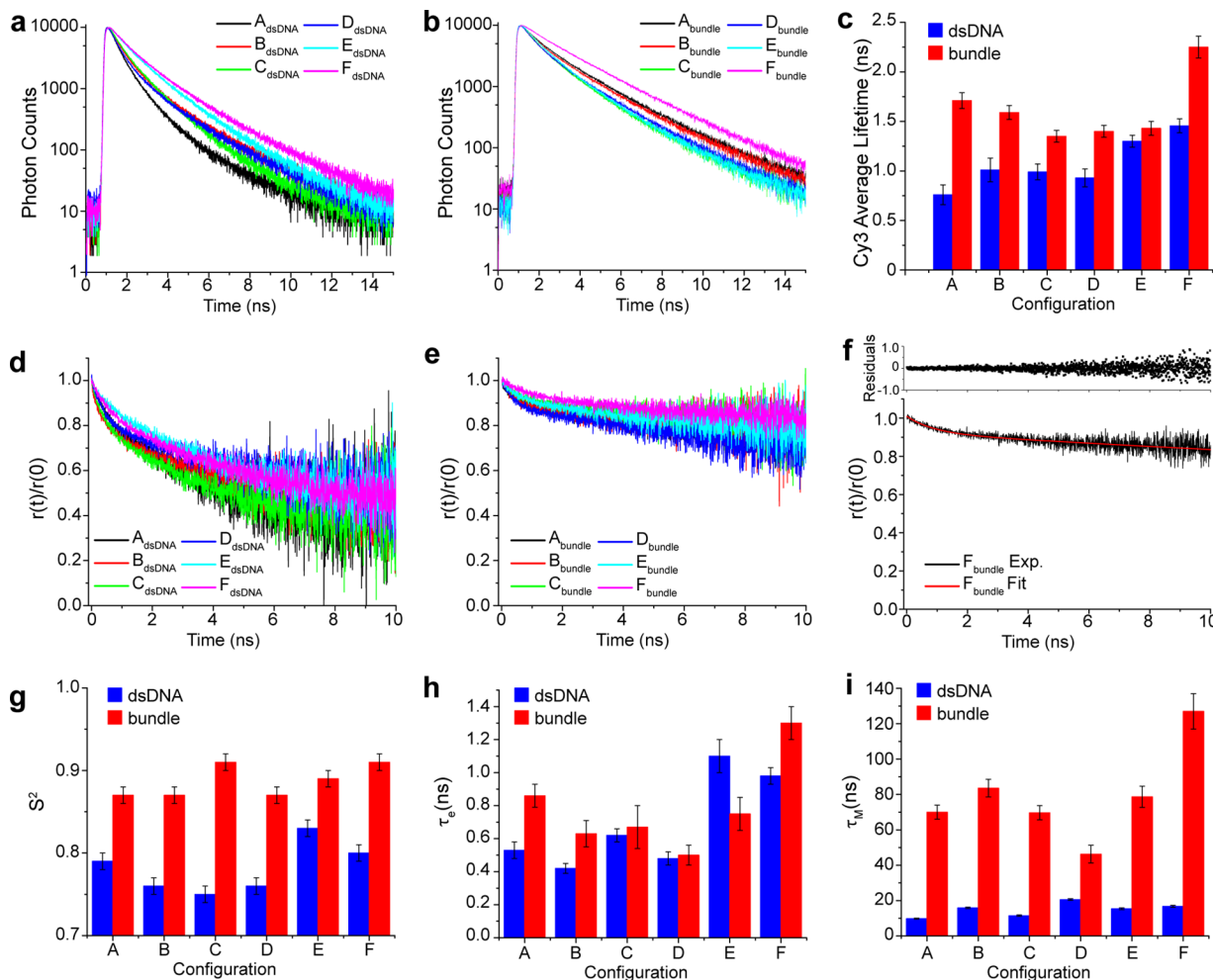


**Figure 4.** Experimental Cy3 time-resolved fluorescence curves and extracted time constants. (a) Cy3–dsDNA fluorescence lifetime decays for structures A–F. (b) Cy3–bundle fluorescence lifetime decays for structures A–F. (c) Excited state decay constants for all structures. (d) Cy3–dsDNA time-resolved anisotropy decays for structures A–F. (e) Cy3–bundle time-resolved anisotropy decays for structures A–F. (f) Time-resolved anisotropy decay for  $F_{\text{bundle}}$  (black) and fit to the data using eq 3 (red) and residuals from fitting shown above. (g–i) Comparison of  $S^2$ ,  $\tau_e$ , and  $\tau_M$  for all structures.

corresponding duplex with the increase in  $S^2$  ranging from 7–20%. The largest  $S^2$  value of 0.91 occurred for the  $F_{\text{bundle}}$ .

To summarize, the main observations from the spectroscopy are: (1) absorption and emission spectra for the bundles are red-shifted with respect to dsDNA, (2) fluorescence and anisotropy lifetimes for the bundles are longer than for dsDNA, and (3)  $S^2$  values are larger for the bundles than for dsDNA. As discussed next in detail, the likely explanation for these observations is that the bundles generally provide a more confining microenvironment surrounding the Cy3 dye.

The red-shifted absorption spectra of the Cy3 in the bundles are likely due to increased Cy3–DNA interactions. This interpretation is supported by results from the literature where the absorption spectra of cyanine dyes have been found to undergo a red shift in the presence of DNA due to interactions with the DNA base stack.<sup>50</sup> It is also possible that a more restrictive environment forces the Cy3 into a more planar configuration, which would produce a red shift from increased  $\pi$ -electron conjugation.

The observation of longer Cy3 fluorescence lifetimes for the bundles is also consistent with a more confining microenvironment. Cy3 is known to undergo a trans-to-cis isomerization about the polymethine bridge following photoexcitation to the

S1 electronic state.<sup>34</sup> When Cy3 is free in solution, photoisomerization dominates the excited state relaxation, resulting in a rapid 180 ps decay time and a low fluorescence quantum yield.<sup>34</sup> When the Cy3 is attached to DNA, photoisomerization is hindered due to the tendency of the Cy3 to interact with the DNA, resulting in increased fluorescence lifetimes.<sup>33,34</sup> The even longer fluorescence lifetimes when Cy3 is attached to the bundle suggest that the photoisomerization is further suppressed by the increased interactions with the bundle. The relative increase in the lifetime is largest for case A. For  $A_{\text{dsDNA}}$ , the single 5' attachment (with the end base removed) permits a greater degree of Cy3 motion external to the duplex compared to  $A_{\text{bundle}}$  where the DNA extends underneath the Cy3 attachment point. Apparently, the increased interaction with DNA restricts the ability of Cy3 to undergo rotation about the methine bridge in the S1 state, resulting in a longer fluorescence lifetime for  $A_{\text{bundle}}$ . In contrast, there is only a relatively small difference in fluorescence lifetimes for case E. Here, Cy3 is doubly attached to both structures and is far away from the crossover site in  $E_{\text{bundle}}$ . The similar fluorescence lifetimes (and similar  $\lambda_{\text{abs}}^{\text{peak}}$ ) suggest that the local microenvironment is similar for  $E_{\text{bundle}}$  and  $E_{\text{dsDNA}}$ . Finally,  $F_{\text{bundle}}$

exhibited the longest fluorescence lifetime of  $2.25 \pm 0.10$  ns, representing a >60% increase in lifetime relative to  $A_{\text{dsDNA}}$ ,  $E_{\text{bundle}}$ , and  $F_{\text{dsDNA}}$ . This observation correlates with the increased red shift of the  $F_{\text{bundle}}$  absorption spectrum and indicates that the Cy3 photoisomerization is further suppressed at the crossover site. These observations may be related to Cy3 experiencing an increase in tension when doubly attached at the crossover site (see Figure 2F). This interpretation is consistent with previous work<sup>31</sup> where MD simulations predicted a distortion of the Holliday junction geometry in DNA origami structures due to tension at the crossover region.

As noted above, the increase in  $S^2$  for the bundles relative to dsDNA is in the range of 7–20%. This modest increase may be related to the tendency of Cy3 to interact with DNA, which is already significant when Cy3 is attached to the duplex. For end-labeled A–D structures, the relative increase in  $S^2$  for the bundles is greatest. This is consistent with the generally higher flexibility of end-labeled Cy3 compared to internal double attachment (E, F). The relatively high  $S^2$  for the  $F_{\text{bundle}}$  is consistent with the notion of increased tension at the crossover site. Because the Cy3–bundle anisotropies still exhibit a short time decay  $\tau_e$ , there remains a small fraction of the bundle ensemble where Cy3 retains a relatively high degree of rotational freedom. However, at the level of noise in the anisotropy measurement, it is difficult to say whether there are systematic trends in the value of  $\tau_e$  across the bundle structures. On the other hand, all structures (A–F) show much larger  $\tau_M$  for the bundles. This long-time Cy3 anisotropy decay could arise from rigid-body tumbling of the entire macromolecule or it could be associated with some internal motion of the DNA with the Cy3 again following along. To estimate the rigid-body behavior, one can model the DNA structures as prolate spheroids with one semiaxis ( $a$ ) much longer than the other ( $b$ ). Under the assumption  $a^2 \gg b^2$ , there exist analytical approximations for the rotational diffusion (defined in Figure S4), and the Stokes–Einstein predictions so derived for the time constants of rotation along the two axes (in a water solvent)— $\tau_R(a)$  and  $\tau_R(b)$ —are given in Table 1.<sup>51</sup>

**Table 1. Rigid-Body Diffusion Analysis of dsDNA and DNA Bundle in Terms of the Rigid Prolate Spheroid Defined in Figure S4**

	$2a$	$2b$	$\tau_R(a)$	$\tau_R(b)$
25 bp dsDNA	8.8 nm	2 nm	36 ns	7 ns
45 bp dsDNA	15.4 nm	2 nm	170 ns	14 ns
DNA bundle	80 nm	20 nm	20 $\mu$ s	7 $\mu$ s

In Table 1, the 25 bp dsDNA corresponds to the A, C, and E duplexes while 45 bp dsDNA represents the B, D, and F duplexes. For dsDNA (A–F), the short-axis rigid-body rotational decay times  $\tau_R(b)$  are of the same order as the experimental  $\tau_M$  (Table S4); thus, it is likely that this motion of the DNA dominates the observed long-time Cy3 anisotropy decay. In contrast, that the longer rotational diffusion times predicted for the bundles (microseconds) are much longer than for the measured  $\tau_M$ 's means that the rigid-body tumbling motion of the bundles is not responsible for the long-time Cy3 anisotropy decay. Instead, we suggest that this decay is associated with the internal collective modes of the bundle.

**MD Simulations of the Dye Motion.** To better understand how a DNA bundle can confine a resident Cy3 dye, we performed a number of atomistic MD simulations. In

particular, we simulated bundle versions of cases A, E, and F with  $A_{\text{bundle}}$  exemplifying the situation of an end-attached Cy3 and E and F looking at internal double-attached Cy3 situated either away from ( $E_{\text{bundle}}$ ) or at a crossover site ( $F_{\text{bundle}}$ ). We compared these bundle cases with simulations for  $A_{\text{dsDNA}}$  and  $E_{\text{dsDNA}}$  as a way of exploring the physical reasons for the large differences between the  $\tau_M$ 's observed for dsDNAs and bundles.

The MD simulations were carried out as described in the Materials and Methods section. Initially, we chose to use the TIP3P model for water; however, this was found to produce anisotropy transients that were much faster than we observed in the experiment. We note previous work on dye-conjugated proteins has found similar discrepancy between experiment and MD simulation.<sup>52</sup> We therefore tested alternative water models, and of these selected TIP4P-Ew because it yielded free Cy3 anisotropy dynamics closest to that measured experimentally (Figure S5).<sup>34</sup>

As a first set of MD simulations, we analyzed  $A_{\text{dsDNA}}$  and  $E_{\text{dsDNA}}$ . In each case, a total of 500 ns was simulated, and from the final 400 ns (chosen to avoid any initial unphysical transient), we extracted the anisotropy dynamics using

$$r(t)/r(0) = \langle P_2[\hat{\mu}(t) \cdot \hat{\mu}(0)] \rangle \quad (4)$$

where  $P_2(x)$  is the second Legendre polynomial

$$P_2(x) = (3x^2 - 1)/2 \quad (5)$$

$\hat{\mu}(t)$  is the normalized transition dipole vector pointing along the long axis of the Cy3 and the brackets indicate an ensemble average (which is approximated by a time average). Considering the complexity of the full DNA–dye system (including water and counterions), the MD prediction for the anisotropy dynamics agrees remarkably well with the experiment (Figure S6). This agreement translates into short ( $\tau_e$ ) and long ( $\tau_M$ ) relaxation times as well as  $S^2$  values (Table S5) derived from biexponential curve fitting (eq 3) that are also in good agreement with the experimental values.

As we have noted, the long relaxation time constant  $\tau_M$  can arise from the overall tumbling of the DNA structure and/or from internal collective motions of the DNA structure. The rotational diffusion model outlined earlier suggested that as the DNA structure grows larger (25 bp dsDNA < 45 bp dsDNA ≪ DNA bundle), its rigid-body rotation slows to the point that internal DNA modes dominate  $\tau_M$ . To look for this behavior in the MD, we analyzed the MD-predicted anisotropy relaxation of  $A_{\text{dsDNA}}$  and  $E_{\text{dsDNA}}$  in both lab and DNA reference frames. Using the lab frame means that all molecular motions of the dye are included, namely, those associated with the tumbling of the DNA, the internal motions of the DNA (including torsional and bending motions), and motions of the dye relative to the DNA. The DNA frame instead follows the tumbling of the DNA and so eliminates this contribution to the dye motion. Figure S6 summarizes the results, and Table S6 compares the values of  $S^2$ ,  $\tau_e$ , and  $\tau_M$  derived from the dynamics. We observe that  $S^2$  is largely unaffected when analyzed in the DNA frame. Furthermore, the values of  $\tau_e$  in the DNA frame remain within 15% of the lab-frame values. Clearly, the DNA frame reveals a slow component in the Cy3 dynamics that can only be due to Cy3 coupling to internal modes of the duplex. The internal dynamics appear much slower for  $E_{\text{dsDNA}}$  ( $\tau_M \sim 120$  ns) than for  $A_{\text{dsDNA}}$ . This result is due in part to the more rigid double attachment of the Cy3 to the DNA. In contrast, the relative flexibility of the single 5'

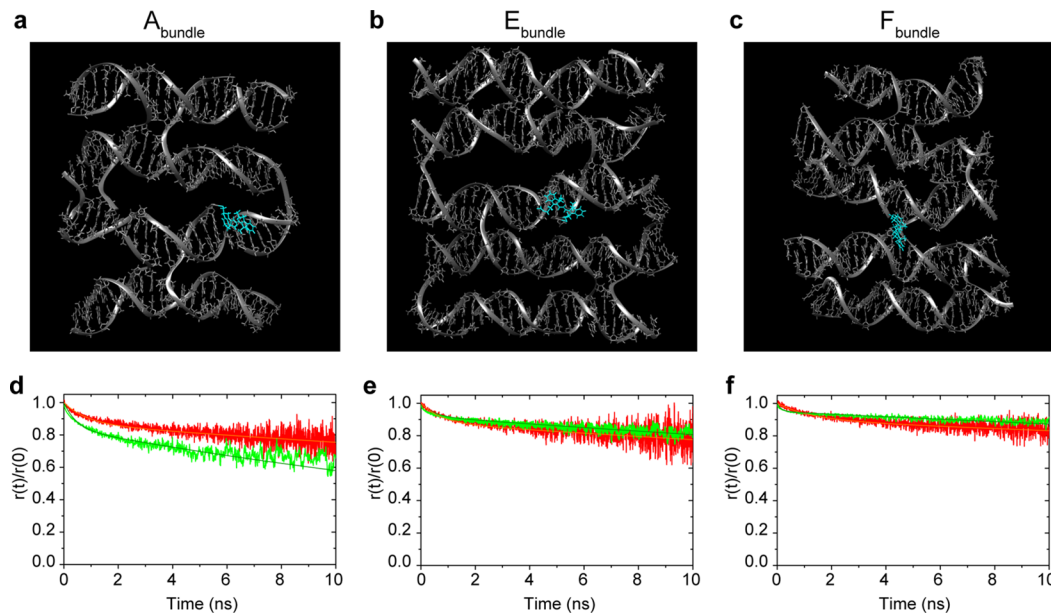


**Figure 5.** (a–c) Snapshots of the local bundle structures (A, E, and F, respectively) from the MD simulations. The position of the Cy3 molecule is shown in cyan color. (d–f) Comparison of simulated (green curves) and experimental (red curves) normalized time-resolved anisotropy for  $A_{\text{bundle}}$  (d),  $E_{\text{bundle}}$  (e), and  $F_{\text{bundle}}$  (f). Solid curves are fits to the data using eq 3.

attachment and of the ends of the duplex give  $A_{\text{dsDNA}}$  its shorter  $\tau_M$ .

Performing analogous MD simulations of the DNA bundle would be computationally expensive as such a model would contain over  $4.6 \times 10^5$  atoms and require  $10^6$  water molecules to generate the aqueous environment. Therefore, we chose instead to simulate just a portion of the bundle containing the Cy3 dye and its surrounding DNA environment. The remainder of the DNA bundle was assumed fixed, an assumption that is in agreement with the prediction of the rigid-body diffusion model—in particular, that the microsecond long tumbling motion of the bundle is too slow to affect the fluorescence anisotropy dynamics. Figure 5a–c shows representative snapshots of the  $A_{\text{bundle}}$ ,  $E_{\text{bundle}}$ , and  $F_{\text{bundle}}$  portions that were simulated, and Figure 5d–f shows the comparison of the MD-determined anisotropy dynamics with the experimental measurement; the associated values of  $S^2$ ,  $\tau_e$ , and  $\tau_M$  are listed in Table 2. Qualitative agreement between

The MD simulations were also used to examine a variation of the  $F_{\text{bundle}}$ , which is referred to as the  $G_{\text{bundle}}$  and that had the Cy3 dye inserted between the crossover bases rather than replacing one base, a configuration explored in Cy5 previously (Figure S7a).<sup>32</sup> The G configuration ensures that all the bases at the crossover site are fully hybridized and thus is expected to yield a more stable structure that might provide enhanced confinement of the dye motion. The results (Figure S7b and Table S7) support this idea with the  $S^2$  value found to be larger than for the A, E, or F bundles and the dye relaxation times are longer. Whether comparable dye dynamics are demonstrable in experiments will be tested in the future.

The anisotropy decay comes particularly from fluctuations in the dye orientation and it is useful to examine this aspect directly using the MD simulations. Using the maps shown in Figure 6, we compared the MD-computed distributions of the dye orientations in bundles ( $A_{\text{bundle}}$  and  $E_{\text{bundle}}$ ) and dsDNA ( $A_{\text{dsDNA}}$  and  $E_{\text{dsDNA}}$ ) structures with the color corresponding to the probability of any given orientation being realized. The largest difference occurs between  $A_{\text{dsDNA}}$  and  $A_{\text{bundle}}$  where the central part of the distribution is much narrower for  $A_{\text{bundle}}$  (Figure 6b). For both  $A_{\text{dsDNA}}$  and  $A_{\text{bundle}}$ , there are wide ranges of orientations with lower probability (red color), a result of the more flexible single attachment design. However, MD snapshots (Figure S8) show that the most likely dye orientations in  $A_{\text{bundle}}$  (blue region of Figure 6) are aligned with the DNA major groove, whereas the less likely orientations (Figure 6, red region) have the Cy3 released from the groove and are no longer aligned. The more localized orientation distribution of  $A_{\text{bundle}}$  is made possible by the Cy3's flexible linker giving the dye the freedom to access the DNA groove. Thus, a less restrictive design results in a more constrained dye, as was seen in the simpler situation of ref 32 noted in the Introduction. In contrast, the orientation distributions for  $E_{\text{dsDNA}}$  and  $E_{\text{bundle}}$  are fairly similar (Figure 6c), with the  $E_{\text{bundle}}$  showing a slightly wider distribution. This may be due to increased internal fluctuations of the bundle in regions in between crossover sites. Finally, as shown in Figure

**Table 2. MD-Derived Anisotropy Relaxation Time Constants and  $S^2$  of  $A_{\text{bundle}}$ ,  $E_{\text{bundle}}$ , and  $F_{\text{bundle}}$**

	$A_{\text{bundle}}$		$E_{\text{bundle}}$		$F_{\text{bundle}}$	
	MD	expt.	MD	expt.	MD	expt.
$S^2$	0.84	0.87	0.92	0.89	0.95	0.91
$\tau_e$	0.47 ns	0.86 ns	0.29 ns	0.75 ns	0.16 ns	1.2 ns
$\tau_M$	27 ns	70 ns	76 ns	79 ns	118 ns	127 ns

the simulation and the experiment is seen, with the correspondence especially good for the values of  $S^2$ , while the MD simulations tended to underestimate  $\tau_e$ . The MD simulations qualitatively reproduced the ordering of  $\tau_M$  for A, E, and F observed in the experiment:  $\tau_M(A) < \tau_M(E) < \tau_M(F)$ . Moreover, the overall agreement between the experimental and simulated values of  $\tau_M$  supports the notion that long relaxation times in the DNA bundle anisotropy are largely associated with slower internal modes of the bundle.

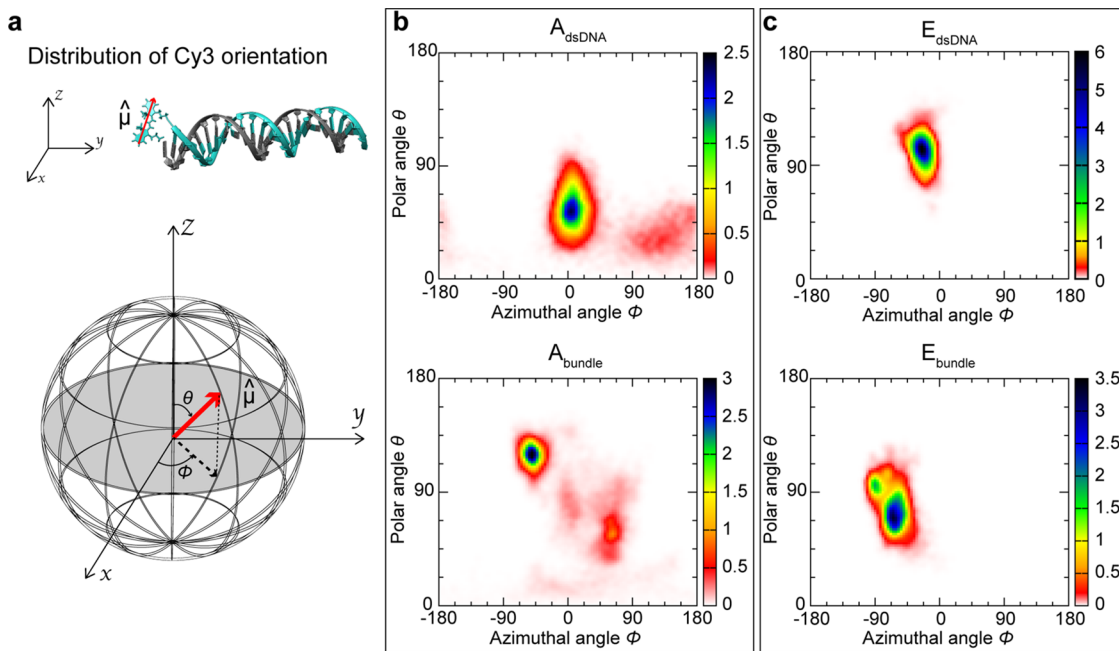


**Figure 6.** Color maps showing the distribution of the normalized Cy3 transition dipole vector derived from the MD simulation. (a) Description of the dipole orientation angles relative to the duplex. Dipole distribution for (b)  $A_{dsDNA}$  and  $A_{bundle}$  and (c)  $E_{dsDNA}$  and  $E_{bundle}$ . The color bars on the right of each map represent the frequency with which the vector is oriented at polar angle  $\theta$  and azimuthal angle  $\varphi$ . Blue colors represent a relatively high occurrence frequency and red colors represent a relatively low occurrence frequency.

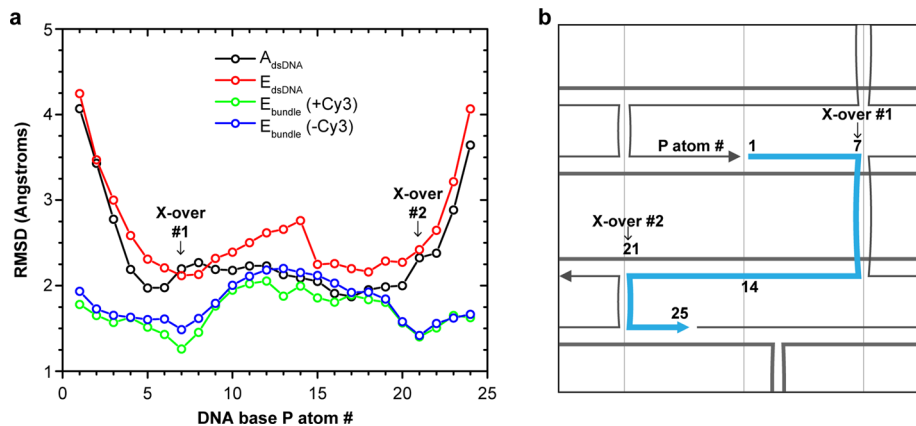


**Figure 7.** (a) RMSD fluctuations derived from MD simulation for  $E_{bundle}$ ,  $A_{dsDNA}$ , and  $E_{dsDNA}$  structures. (b) The bundle region that was simulated. The P atom RMSD fluctuations were calculated for the 25 atoms along the blue staple strand.

S9, the orientation distributions of  $G_{dsDNA}$  and  $G_{bundle}$  are compared in a slightly different way by plotting the distribution of Cy3 dipole angles from the MD simulations on a unit sphere. In this case,  $G_{bundle}$  shows a significantly narrower orientation distribution than  $G_{dsDNA}$ . Thus, the MD simulations indicate that the DNA bundle is no better than a duplex for constraining the orientation of internally attached Cy3s, except when the fully hybridized crossover design of the  $G_{bundle}$  is used.

The MD simulations also provide insight into the site-to-site fluctuations in the bundles and dsDNA where the sites are considered as individual nucleotides. Figure 7a shows the comparison of the root mean square deviation (RMSD) position of the P atom at each site along the staple strand in  $E_{bundle}$  (shown in blue in Figure 7b) and along  $A_{dsDNA}$  and  $E_{dsDNA}$ . For the dsDNA duplexes, the fluctuations are largest near the ends (Figure 7a) and drop rapidly as one moves

inward. A slight exception is  $E_{dsDNA}$ , which shows a small rise in fluctuations near the center of the strand that is likely due to its doubly attached Cy3 that replaces a central nucleobase and makes the duplex less rigid by interrupting base stacking. Comparing the analogous P atom fluctuations along the staple strand of  $E_{bundle}$  (Figure 7a), we see an overall reduction in fluctuations when compared to the duplexes, and especially near the ends of the staple strand, which are now much more constrained due to interactions with neighboring staple strand termini. In addition, at the crossover sites, there are clear minima in the fluctuations indicating that these regions are especially stable. The RMSD values at the two crossover sites have similar values, which suggest that structural effects play a greater role than the local sequence in this region. The small rise as one moves to the center of the strand is not dye-related (as shown by the control simulation with no dye) but arises

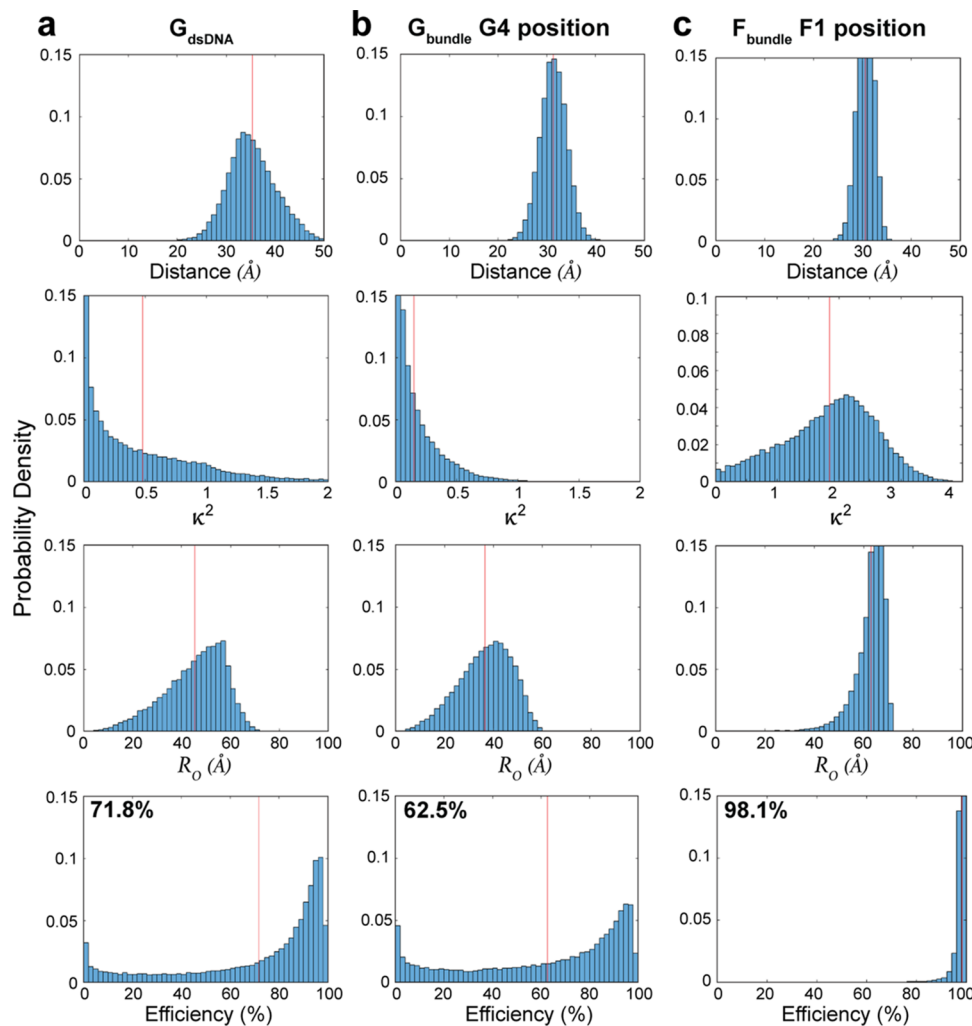


**Figure 8.** Predicted probability densities of distance ( $\text{\AA}$ ), orientation ( $\kappa^2$ ),  $R_0$  ( $\text{\AA}$ ), and FRET efficiency ( $E$ ) in (a)  $G_{\text{dsDNA}}$ , (b)  $G_{\text{bundle}}$  site G4, and (c)  $F_{\text{bundle}}$  site F1. The vertical red lines indicate the weighted average for each quantity.

simply because the central region is less constrained than the crossovers.

The experimental trends observed in the Cy3 fluorescence lifetimes for the dsDNAs and bundles correlate with the foregoing observations regarding the size of the P atom fluctuations. For example, the shortest lifetimes occur for end-attached Cy3s in dsDNA structures ( $A_{\text{dsDNA}}-D_{\text{dsDNA}}$ ) where the P atom fluctuations are the largest. Likewise, the internally attached Cy3s in the dsDNA samples ( $E_{\text{dsDNA}}$  and  $F_{\text{dsDNA}}$ ) are at sites with smaller P atom fluctuations and longer lifetimes are indeed seen. In the case of the bundles, smaller P atom fluctuations (when compared to the dsDNA analogues) occur at the ends of the staple strand ( $A_{\text{bundle}}-D_{\text{bundle}}$ ), and at the crossover site ( $F_{\text{bundle}}$ ), and each of these cases shows longer fluorescence lifetimes than the corresponding dsDNA structures. Furthermore, in cases when the P atom fluctuations are similar for both the dsDNA and bundle, such as in the middle of the DNA duplex ( $E_{\text{dsDNA}}$ ) and in the middle of the staple strand ( $E_{\text{bundle}}$ ), the fluorescence lifetimes are correspondingly similar. Presumably, all of these observations are explained by the fact that the steric constraints that reduce P atom fluctuations also constrain the Cy3 dye and suppress its photoisomerization.

**FRET Simulations.** The agreements between the experiment and MD predictions given in Figure 5 represent a partial validation of the MD model, and thereby also serve to support our simulation results of the previous subsection that suggested that the DNA bundle constrains the motion of an attached dye (Cy3) more than dsDNA. These differences are made especially evident in the plots of the Cy3 dipole and linker angles (Figure S9). The MD analysis does not address, however, whether this level of constraint approaches what is needed to benefit LH applications. A full answer would require a thorough experimental and computational investigation that is beyond the scope of this work. Here, we limit our study to FRET simulations that incorporate the MD-simulated dye motions and provide an initial evaluation of the degree to which use of the bundle as a scaffold might improve energy transfer efficiency over that obtained with the duplex.

For these FRET simulations, we assume that the Förster approximation is valid and employ a Monte Carlo procedure to compute the energy transfer efficiency between two dyes, here assumed to be Cy3 and Cy5, as an average over an ensemble in which the particular dye positions and orientations are assumed distributed as computed by the MD over time. For any particular instantiation, the FRET efficiency  $E$  is related to the interdye distance  $R$  by the Förster formula<sup>53</sup>

$$E = \frac{1}{1 + (R/R_0)^6} \quad (6)$$

where  $R_0$  is the Förster distance calculated as<sup>53</sup>

$$R_0 = \left( \frac{9(\ln 10)}{128 \pi^5 N_A} \frac{\kappa^2 Q_D}{n^4} \int F_D(\lambda) \epsilon_A(\lambda) \lambda^4 d\lambda \right)^{1/6} \quad (7)$$

In eq 7,  $Q_D$  is the fluorescence quantum yield,  $N_A$  is Avogadro's number,  $n$  is the refractive index,  $F_D$  is the normalized emission spectrum of the donor,  $\epsilon_A$  is the molar absorptivity of the acceptor, the integral is over the wavelength,  $\lambda$ . The dye orientations (i.e., the transition dipole moments  $\hat{\mu}_A$  and  $\hat{\mu}_D$ ) enter through the dipole orientation factor

$$\kappa^2 = \hat{\mu}_A \cdot \hat{\mu}_D - 3(\hat{\mu}_A \cdot \hat{R})(\hat{\mu}_D \cdot \hat{R}) \quad (8)$$

where all of the vectors are normalized. In addition to the ergodic theorem, this approach has an implicit static assumption that the FRET occurs on a faster time scale than the dye motions. It is important to note that our goal in these calculations is not to show that the bundle always provides better dye control and photophysical performance than does dsDNA, but rather to investigate whether there are favored locations in the bundle that can provide such control. This means that a comparison based on single FRET simulations of a dye pair in a bundle versus that in dsDNA would not be sufficient, and instead, we need FRET simulations for dye pairs in many different positions. To this end, we located the Cy3 donor at any of the locations discussed in the previous subsection for which we already have the needed position/orientation histories. To avoid the computationally heavy burden of performing many new MD simulations, for the Cy5 acceptor, we instead approximate their position/orientation histories in the following way. First, we identified various Cy5 attachment points in the bundles (specifically the A, F, and G bundles) and the dsDNA (specifically cases A and G), all within 27–31 Å from the Cy3, and recorded the MD histories of these positions (Figure S10). Then, we assumed the histories of each Cy5's motion relative to its attachment point and its dipole orientation can be approximated by the corresponding Cy3 behavior uncorrelated in time and rotated to account for the different local orientations of the DNA.

Using this approach, we performed many FRET simulations of Cy3–Cy5 pairs attached either to the dsDNA or to the bundle, and we here present a few highlights that convey the main conclusions. The results are displayed in the plots of the distributions of  $R$ ,  $\kappa^2$ ,  $R_0$ , and  $E$  for various Cy3–Cy5 pairs shown in Figure 8 and Figure S11. Again, these are for a single structure collected over time but are presumed to represent a snapshot of an ensemble of structures in equilibrium. In all dsDNA cases, the distributions looked much like those shown in Figure 8a with the interdye distances  $R$  broadly distributed, indicating that the dsDNA does not significantly constrain the dyes. The  $\kappa^2$  values are seen to be “isotropically”<sup>54</sup> distributed with low values favored because of the nature of eq 8 and with an average of about 0.5; this causes the  $R_0$  distribution to be broadened as well. With regard to the FRET, the distributions in  $R$  and  $R_0$  in turn cause the transfer efficiencies of the dsDNA-scaffolded pair to be likewise widely distributed with an average of about 72% (see Figure 8a). The analogous plots for two specific Cy3–Cy5 pairs in the G and F bundles are shown in Figure 8b,c (see also Figure S11 for similar plots for

all the other pair locations in bundles), and we find that the distributions of  $R$  and  $\kappa^2$  are considerably narrower than in the dsDNA case. In part, the narrower distributions of  $R$  for the bundles are related to smaller RMSD fluctuations than in dsDNA (Figure 7). However, the FRET efficiency for the  $G_{\text{bundle}}$  site G4 does not seem to be much different from the corresponding  $G_{\text{dsDNA}}$  site, whereas for the  $F_{\text{bundle}}$  site F1, we see markedly different results with a very high transfer efficiency (98%). This suggests that the particular Cy3 and Cy5 locations shown in Figure 8c are especially favorable and that the constraints provided by those sites within the  $F_{\text{bundle}}$  are paying off. Just as interesting is the fact that the  $G_{\text{bundle}}$  site G4 (Figure 8b), also motionally constrained as revealed by the narrowed  $R$  and  $\kappa^2$  distributions, instead shows a much lower average  $\kappa^2$  ( $\sim 0.15$ ) and a reduced FRET efficiency, which evidences that in this case the constraints hold the dye pair in an unfavorable orientation for FRET. One final point is that the bundle does not always impose such constraints—see the results for other positions in the A, G, and F bundles in the Supporting Information (Figure S11 b–k). Similarly, the three other equidistant sites within the  $F_{\text{bundle}}$  alone (Figure S11 f–h) do not match the site F1 shown in Figure 8c. We thus conclude that properly chosen dye locations in the bundle are indeed capable of constraining the dye orientations to a degree sufficient to provide significant photophysical benefits, and as a result, a careful design in the future could produce a high-performing FRET network.

## CONCLUSIONS

We have used both experiment and MD simulations to characterize the ability of a DNA origami bundle to constrain the position and orientation of a chemically attached Cy3 dye. The experiments investigated Cy3 attached at different sites within a localized region of the 30-helix bundle that was predicted by coarse-grained conformational dynamics to have relatively high rigidity. The dye attachment sites included flexible single covalent attachment at the 5' and 3' ends of DNA strands, as well as more rigid internal attachment using double covalent linkage of Cy3 to DNA. In this way, we were able to explore the effects of the dye linkage type and the site-dependent DNA nanostructure rigidity on Cy3 rotational fluctuations. Time-resolved fluorescence anisotropy experiments showed generally longer rotational dynamics for Cy3 attached to DNA bundles compared to simple dsDNA analogues. Atomistic MD simulations of Cy3 rotational dynamics in DNA bundles and dsDNA showed good agreement with the experiment. In addition to confirming that the bundle constrains Cy3 rotational fluctuations, MD led to an understanding of the “slow” Cy3 anisotropy dynamics as coupling of the dye to the internal fluctuations of DNA, either through groove binding or via the covalent attachment to the DNA backbone. MD also helped to answer whether the DNA origami can constrain the position and orientation of dye molecules. To this end, the MD data were used to simulate the FRET efficiency for Cy3–Cy5 pairs in DNA bundles and in dsDNA. The FRET simulations showed that, indeed, in specific cases, the bundle can constrain the dye position and orientation sufficiently that the transfer efficiency will be significantly augmented. At the same time, the majority of the investigated dye–dye configurations showed a lower FRET efficiency because the bundle constrained the dyes on average in an unfavorable orientation, which is consistent with eq 8, and the arbitrarily oriented dye transition dipoles tend to

produce small values of  $\kappa^2$ . While not desirable, this further confirms the ability of the DNA bundle to constrain the dye motion. Thus, the main conclusion of this work is that the DNA origami bundle can sufficiently constrain the Cy3 dye position and orientation to purposefully influence the photophysical properties, including excited state lifetime and energy transfer efficiency.

DNA origami has gained interest as scaffolds to organize dye molecules because it can be assembled into arbitrary 3D shapes deemed suitable for specific applications and it contains a high density of chemically addressable sites to place dyes. While the results of this work have demonstrated that the DNA origami can constrain the Cy3 dye position and orientation, it is not yet known whether the degree of constraint found here is sufficient to enable photonic applications such as synthetic LH and excitonic circuitry for information processing.<sup>55,56</sup> Realizing such applications will likely require finding ways to further improve the control of the dye position and orientation. These might include exploring the use of cross-linking DNA<sup>57</sup> and using peptide nucleic acids<sup>58</sup> to enhance the rigidity of the DNA origami scaffold. In addition, exploring structural designs that modulate the strain in DNA origami have been suggested as an approach to increase rigidity.<sup>59</sup> While not explored in this work, it is worth mentioning that the attachment sites at the Holliday junctions in the DNA origami provide an opportunity to explore dye–dye interactions in the strong coupling regime.<sup>11</sup> Finally, the degree to which other dyes and dye classes can be constrained by the DNA origami likely depends on properties such as dye hydrophobicity, electrostatic interactions between the dye and DNA, and the type of attachment chemistry available. We anticipate that other cyanine dyes Cy3.5, Cy5, and Cy5.5 would be constrained by the DNA origami to a similar degree as Cy3 because as hydrophobic dyes they also tend to interact with the DNA base stacking region and they use the same attachment chemistry. The role of dye hydrophobicity could be tested by attaching substituents to the cyanine backbone that alter the dye's hydrophobicity/hydrophilicity.

## ■ ASSOCIATED CONTENT

### SI Supporting Information

The Supporting Information is available free of charge at <https://pubs.acs.org/doi/10.1021/acs.jpcc.0c09258>.

Diagram and list of sequences of the DNA bundle, steady-state spectra, rigid-body diffusion model, supporting MD analyses, Cy3 linker and dipole angle distributions, and predicted FRET parameters of remaining structures ([PDF](#))

## ■ AUTHOR INFORMATION

### Corresponding Author

**Joseph S. Melinger** — *Electronics Science and Technology Division, U.S. Naval Research Laboratory, Washington, D.C. 20375, United States; [orcid.org/0000-0002-2452-5245](#); Email: [joseph.melinger@nrl.navy.mil](mailto:joseph.melinger@nrl.navy.mil)*

### Authors

**Divita Mathur** — *College of Science, George Mason University, Fairfax, Virginia 22030, United States; Center for Bio/Molecular Science and Engineering, U.S. Naval Research Laboratory, Washington, D.C. 20375, United States; [orcid.org/0000-0002-3537-7292](#)*

**Young C. Kim** — *Materials Science and Technology Division, U.S. Naval Research Laboratory, Washington, D.C. 20375, United States*

**Sebastián A. Díaz** — *Center for Bio/Molecular Science and Engineering, U.S. Naval Research Laboratory, Washington, D.C. 20375, United States; [orcid.org/0000-0002-5568-0512](#)*

**Paul D. Cunningham** — *Electronics Science and Technology Division, U.S. Naval Research Laboratory, Washington, D.C. 20375, United States; [orcid.org/0000-0002-3602-1503](#)*

**Brian S. Rolczynski** — *Electronics Science and Technology Division, U.S. Naval Research Laboratory, Washington, D.C. 20375, United States; ASEE Postdoctoral Associate, Washington, D.C. 20036, United States*

**Mario G. Ancona** — *Electronics Science and Technology Division, U.S. Naval Research Laboratory, Washington, D.C. 20375, United States*

**Igor L. Medintz** — *Center for Bio/Molecular Science and Engineering, U.S. Naval Research Laboratory, Washington, D.C. 20375, United States; [orcid.org/0000-0002-8902-4687](#)*

Complete contact information is available at:  
<https://pubs.acs.org/10.1021/acs.jpcc.0c09258>

### Author Contributions

The manuscript was written through contributions of all authors. All authors have given approval to the final version of the manuscript.

### Notes

The authors declare no competing financial interest.

## ■ ACKNOWLEDGMENTS

The authors gratefully acknowledge funding from the Office of Naval Research (ONR), the U.S. Naval Research Laboratory (NRL), and the NRL Nanoscience Institute. B.S.R. acknowledges the American Society for Engineering Education Fellowship (ASEE).

## ■ REFERENCES

- (1) Mathur, D.; Klein, W. P.; Chiriboga, M.; Bui, H.; Oh, E.; Nita, R.; Naciri, J.; Johns, P.; Fontana, J.; Diaz, S. A.; et al. Analyzing Fidelity and Reproducibility of DNA Templatized Plasmonic Nanostructures. *Nanoscale* **2019**, *11*, 20693–20706.
- (2) Kuzyk, A.; Schreiber, R.; Fan, Z.; Pardatscher, G.; Roller, E. M.; Hogele, A.; Simmel, F. C.; Govorov, A. O.; Liedl, T. DNA-Based Self-Assembly of Chiral Plasmonic Nanostructures with Tailored Optical Response. *Nature* **2012**, *483*, 311–314.
- (3) Ma, N.; Minevich, B.; Liu, J.; Ji, M.; Tian, Y.; Gang, O. Directional Assembly of Nanoparticles by DNA Shapes: Towards Designed Architectures and Functionality. *Top Curr. Chem. (z)* **2020**, *378*, 36.
- (4) Klein, W. P.; Thomsen, R. P.; Turner, K. B.; Walper, S. A.; Vranish, J.; Kjems, J.; Ancona, M. G.; Medintz, I. L. Enhanced Catalysis from Multienzyme Cascades Assembled on a DNA Origami Triangle. *ACS Nano* **2019**, *13*, 13677–13689.
- (5) Klein, W. P.; Schmidt, C. N.; Rapp, B.; Takabayashi, S.; Knowlton, W. B.; Lee, J.; Yurke, B.; Hughes, W. L.; Graugnard, E.; Kuang, W. Multiscroll DNA Origami Nanoparticle Waveguides. *Nano Lett.* **2013**, *13*, 3850–3856.
- (6) Stein, I. H.; Steinhauer, C.; Tinnefeld, P. Single-Molecule Four-Color FRET Visualizes Energy-Transfer Paths on DNA Origami. *J. Am. Chem. Soc.* **2011**, *133*, 4193–4195.

- (7) Dutta, P. K.; Varghese, R.; Nangreave, J.; Lin, S.; Yan, H.; Liu, Y. DNA-Directed Artificial Light-Harvesting Antenna. *J. Am. Chem. Soc.* **2011**, *133*, 11985–11993.
- (8) Buckhout-White, S.; Spillmann, C. M.; Algar, W. R.; Khachatrian, A.; Melinger, J. S.; Goldman, E. R.; Ancona, M. G.; Medintz, I. L. Assembling Programmable FRET-Based Photonic Networks Using Designer DNA Scaffolds. *Nat. Commun.* **2014**, *5*, 5615.
- (9) Banal, J. L.; Kondo, T.; Veneziano, R.; Bathe, M.; Schlau-Cohen, G. S. Photophysics of J-Aggregate-Mediated Energy Transfer on DNA. *J. Phys. Chem. Lett.* **2017**, *8*, 5827–5833.
- (10) Boulais, E.; Sawaya, N. P. D.; Veneziano, R.; Andreoni, A.; Banal, J. L.; Kondo, T.; Mandal, S.; Lin, S.; Schlau-Cohen, G. S.; Woodbury, N. W.; et al. Programmed Coherent Coupling in a Synthetic DNA-Based Excitonic Circuit. *Nat. Mater.* **2018**, *17*, 159–166.
- (11) Cannon, B. L.; Patten, L. K.; Kellis, D. L.; Davis, P. H.; Lee, J.; Graugnard, E.; Yurke, B.; Knowlton, W. B. Large Davydov Splitting and Strong Fluorescence Suppression: An Investigation of Exciton Delocalization in DNA-Templated Holliday Junction Dye Aggregates. *J. Phys. Chem. A* **2018**, *122*, 2086–2095.
- (12) Diaz, S. A.; Oliver, S. M.; Hastman, D. A.; Medintz, I. L.; Vora, P. M. Increased Transfer Efficiency from Molecular Photonic Wires on Solid Substrates and Cryogenic Conditions. *J. Phys. Chem. Lett.* **2018**, *9*, 3654–3659.
- (13) Hemmig, E. A.; Creatore, C.; Wunsch, B.; Hecker, L.; Mair, P.; Parker, M. A.; Emmott, S.; Tinnefeld, P.; Keyser, U. F.; Chin, A. W. Programming Light-Harvesting Efficiency Using DNA Origami. *Nano Lett.* **2016**, *16*, 2369–2374.
- (14) Krainer, G.; Hartmann, A.; Schlierf, M. FarFRET: Extending the Range in Single-Molecule FRET Experiments Beyond 10 nm. *Nano Lett.* **2015**, *15*, 5826–5829.
- (15) Nishimura, T.; Ogura, Y.; Tanida, J. Fluorescence Resonance Energy Transfer-Based Molecular Logic Circuit Using a DNA Scaffold. *Appl. Phys. Lett.* **2012**, *101*, 233703.
- (16) Olejko, L.; Bald, I. FRET Efficiency and Antenna Effect in Multi-Color DNA Origami-Based Light Harvesting Systems. *RSC Adv.* **2017**, *7*, 23924–23934.
- (17) Hannestad, J. K.; Gerrard, S. R.; Brown, T.; Albinsson, B. Self-Assembled DNA-Based Fluorescence Waveguide with Selectable Output. *Small* **2011**, *7*, 3178–3185.
- (18) Kownacki, M.; Langenegger, S. M.; Liu, S.-X.; Häner, R. Integrating DNA Photonic Wires into Light-Harvesting Supramolecular Polymers. *Angew. Chem., Int. Ed.* **2019**, *58*, 751–755.
- (19) Kato, T.; Kashida, H.; Kishida, H.; Yada, H.; Okamoto, H.; Asanuma, H. Development of a Robust Model System of FRET Using Base Surrogates Tethering Fluorophores for Strict Control of Their Position and Orientation within DNA Duplex. *J. Am. Chem. Soc.* **2012**, *135*, 741–750.
- (20) Hannestad, J. K.; Sandin, P.; Albinsson, B. Self-Assembled DNA Photonic Wire for Long-Range Energy Transfer. *J. Am. Chem. Soc.* **2008**, *130*, 15889–15895.
- (21) Zhou, X.; Mandal, S.; Jiang, S.; Lin, S.; Yang, J.; Liu, Y.; Whitten, D. G.; Woodbury, N. W.; Yan, H. Efficient Long-Range, Directional Energy Transfer through DNA-Templated Dye Aggregates. *J. Am. Chem. Soc.* **2019**, *141*, 8473–8481.
- (22) Pan, K.; Boulais, E.; Yang, L.; Bathe, M. Structure-Based Model for Light-Harvesting Properties of Nucleic Acid Nanostructures. *Nucleic Acids Res.* **2014**, *42*, 2159–2170.
- (23) Scholes, G. D.; Fleming, G. R.; Olaya-Castro, A.; van Grondelle, R. Lessons from Nature About Solar Light Harvesting. *Nat. Chem.* **2011**, *3*, 763–774.
- (24) Brintlinger, T. H.; Buckhout-White, S.; Bassim, N. D.; Mathur, D.; Samanta, A.; Robinson, J. T.; Idrobo, J.-C.; Stroud, R. M.; Goldman, E. R.; Ancona, M. G. Chemical Mapping of Unstained DNA Origami Using STEM/EDS and Graphene Supports. *ACS Appl. Nano Mater.* **2020**, *3*, 1123–1130.
- (25) Benson, E.; Lolaico, M.; Tarasov, Y.; Gadin, A.; Hogberg, B. Evolutionary Refinement of DNA Nanostructures Using Coarse-Grained Molecular Dynamics Simulations. *ACS Nano* **2019**, *13*, 12591–12598.
- (26) Liang, L.; Shen, J. W.; Wang, Q. Molecular Dynamics Study on DNA Nanotubes as Drug Delivery Vehicle for Anticancer Drugs. *Colloids Surf., B* **2017**, *153*, 168–173.
- (27) Maffeo, C.; Yoo, J.; Aksimentiev, A. *De Novo* Reconstruction of DNA Origami Structures through Atomistic Molecular Dynamics Simulation. *Nucleic Acids Res.* **2016**, *44*, 3013–3019.
- (28) Pan, K.; Bricker, W. P.; Ratanalert, S.; Bathe, M. Structure and Conformational Dynamics of Scaffolded DNA Origami Nanoparticles. *Nucleic Acids Res.* **2017**, *45*, 6284–6298.
- (29) Shi, Z.; Castro, C. E.; Arya, G. Conformational Dynamics of Mechanically Compliant DNA Nanostructures from Coarse-Grained Molecular Dynamics Simulations. *ACS Nano* **2017**, *11*, 4617–4630.
- (30) Wozniak, A. K.; Schroder, G. F.; Grubmuller, H.; Seidel, C. A.; Oesterhelt, F. Single-Molecule FRET Measures Bends and Kinks in DNA. *Proc. Natl. Acad. Sci. U. S. A.* **2008**, *105*, 18337–18342.
- (31) Yoo, J.; Aksimentiev, A. In Situ Structure and Dynamics of DNA Origami Determined through Molecular Dynamics Simulations. *Proc. Natl. Acad. Sci. U. S. A.* **2013**, *110*, 20099–20104.
- (32) Mazuski, R. J.; Diaz, S. A.; Wood, R. E.; Lawson, T. L.; Klein, W. P.; Mathur, D.; Melinger, J. S.; Engel, G. S.; Medintz, I. L. Ultra-Fast Excitation Transfer in Cy5 DNA Photonic Wires Displays Dye Conjugation and Excitation Energy Dependency. *J. Phys. Chem. Lett.* **2020**, *11*, 4163–4172.
- (33) Cunningham, P. D.; Khachatrian, A.; Buckhout-White, S.; Deschamps, J. R.; Goldman, E. R.; Medintz, I. L.; Melinger, J. S. Resonance Energy Transfer in DNA Duplexes Labeled with Localized Dyes. *J. Phys. Chem. B* **2014**, *118*, 14555–14565.
- (34) Sanborn, M. E.; Connolly, B. K.; Gurunathan, K.; Levitus, M. Fluorescence Properties and Photophysics of the Sulfoindocyanine Cy3 Linked Covalently to DNA. *J. Phys. Chem. B* **2007**, *111*, 11064–11074.
- (35) Matikonda, S. S.; Hammersley, G.; Kumari, N.; Grabenhorst, L.; Glembockyte, V.; Tinnefeld, P.; Ivanic, J.; Levitus, M.; Schnermann, M. J. Impact of Cyanine Conformational Restraint in the near-Infrared Range. *J. Org. Chem.* **2020**, *85*, 5907–5915.
- (36) Nguyen, B.; Ciuba, M. A.; Kozlov, A. G.; Levitus, M.; Lohman, T. M. Protein Environment and DNA Orientation Affect Protein-Induced Cy3 Fluorescence Enhancement. *Biophys. J.* **2019**, *117*, 66–73.
- (37) Pal, S.; Deng, Z.; Wang, H.; Zou, S.; Liu, Y.; Yan, H. DNA Directed Self-Assembly of Anisotropic Plasmonic Nanostructures. *J. Am. Chem. Soc.* **2011**, *133*, 17606–17609.
- (38) Pettersen, E. F.; Goddard, T. D.; Huang, C. C.; Couch, G. S.; Greenblatt, D. M.; Meng, E. C.; Ferrin, T. E. UCSF Chimera—a Visualization System for Exploratory Research and Analysis. *J. Comput. Chem.* **2004**, *25*, 1605–1612.
- (39) Van Der Spoel, D.; Lindahl, E.; Hess, B.; Groenhof, G.; Mark, A. E.; Berendsen, H. J. Gromacs: Fast, Flexible, and Free. *J. Comput. Chem.* **2005**, *26*, 1701–1718.
- (40) Hornak, V.; Abel, R.; Okur, A.; Strockbine, B.; Roitberg, A.; Simmerling, C. Comparison of Multiple Amber Force Fields and Development of Improved Protein Backbone Parameters. *Proteins* **2006**, *65*, 712–725.
- (41) Wang, J.; Wolf, R. M.; Caldwell, J. W.; Kollman, P. A.; Case, D. A. Development and Testing of a General Amber Force Field. *J. Comput. Chem.* **2004**, *25*, 1157–1174.
- (42) Vega, C.; Abascal, J. L.; Nezbeda, I. Vapor-Liquid Equilibria from the Triple Point up to the Critical Point for the New Generation of TIP\$P-Like Models: TIP4P/Ew, TIP4P/2005, and TIP4P/Ice. *J. Chem. Phys.* **2006**, *125*, No. 034503.
- (43) Hess, B.; Bekker, H.; Berendsen, H. J. C.; Fraaije, J. G. E. M. LINCS: A Linear Constraint Solver for Molecular Simulations. *J. Comput. Chem.* **1997**, *18*, 1463–1472.
- (44) Bussi, G.; Donadio, D.; Parrinello, M. Canonical Sampling through Velocity Rescaling. *J. Chem. Phys.* **2007**, *126*, No. 014101.

- (45) Parrinello, M.; Rahman, A. Polymorphic Transitions in Single Crystals: A New Molecular Dynamics Method. *J. Appl. Phys.* **1981**, *52*, 7182–7190.
- (46) Rothemund, P. W. Folding DNA to Create Nanoscale Shapes and Patterns. *Nature* **2006**, *440*, 297–302.
- (47) Douglas, S. M.; Marblestone, A. H.; Teerapittayanon, S.; Vazquez, A.; Church, G. M.; Shih, W. M. Rapid Prototyping of 3d DNA-Origami Shapes with CaDNAno. *Nucleic Acids Res.* **2009**, *37*, S5001–S5006.
- (48) Lipari, G.; Szabo, A. Effect of Vibrational Motion on Fluorescence Depolarization and Nuclear Magnetic Resonance Relaxation in Macromolecules and Membranes. *Biophys. J.* **1980**, *30*, 489–506.
- (49) Lipari, G.; Szabo, A. Model-Free Approach to the Interpretation of Nuclear Magnetic Resonance Relaxation in Macromolecules. 1. Theory and Range of Validity. *J. Am. Chem. Soc.* **1982**, *104*, 4546–4559.
- (50) Rye, H. S.; Yue, S.; Wemmer, D. E.; Quesada, M. A.; Haugland, R. P.; Mathies, R. A.; Glazer, A. N. Stable Fluorescent Complexes of Double-Stranded DNA with Bis-Intercalating Asymmetric Cyanine Dyes: Properties and Applications. *Nucleic Acids Res.* **1992**, *20*, 2803–2812.
- (51) Berg, H. C., *Random Walks in Biology*, Expanded ed.; Princeton University Press: Princeton, NJ, 1993, 152.
- (52) Schroder, G. F.; Alexiev, U.; Grubmuller, H. Simulation of Fluorescence Anisotropy Experiments: Probing Protein Dynamics. *Biophys. J.* **2005**, *89*, 3757–3770.
- (53) Lakowicz, J. R., *Principles of Fluorescence Spectroscopy*; Springer, 1983.
- (54) Vogel, S. S.; van der Meer, B. W.; Blank, P. S. Estimating the Distance Separating Fluorescent Protein FRET Pairs. *Methods* **2014**, *66*, 131–138.
- (55) Kellis, D. L.; Sarter, C.; Cannon, B. L.; Davis, P. H.; Graugnard, E.; Lee, J.; Pensack, R. D.; Kolmar, T.; Jáschke, A.; Yurke, B.; et al. An All-Optical Excitonic Switch Operated in the Liquid and Solid Phases. *ACS Nano* **2019**, *13*, 2986–2994.
- (56) Sawaya, N. P. D.; Rappoport, D.; Tabor, D. P.; Aspuru-Guzik, A. Excitonics: A Set of Gates for Molecular Exciton Processing and Signaling. *ACS Nano* **2018**, *12*, 6410–6420.
- (57) De Fazio, A. F.; El-Sagheer, A. H.; Kahn, J. S.; Nandakumar, I.; Burton, M. R.; Brown, T.; Muskens, O. L.; Gang, O.; Kanaras, A. G. Light-Induced Reversible DNA Ligation of Gold Nanoparticle Superlattices. *ACS Nano* **2019**, *13*, 5771–5777.
- (58) Nielsen, P. E.; Egholm, M.; Buchardt, O. Peptide Nucleic Acid (PNA). A DNA Mimic with a Peptide Backbone. *Bioconjugate Chem.* **2004**, *5*, 3–7.
- (59) Kim, Y.-J.; Lee, C.; Lee, J. G.; Kim, D.-N. Configurational Design of Mechanical Perturbation for Fine Control of Twisted DNA Origami Structures. *ACS Nano* **2019**, *13*, 6348–6355.